Manipulating motions of elastomer films by electrostatically-controlled aperiodicity

IOP Publishing Smart Materials and Structures
Smart Mater. Struct. **25** (2016) 125012 (13pp) doi:10.1088/0964-1726/25/12/125012

Manipulating motions of elastomer films by electrostatically-controlled aperiodicity

Gal Shmuel[1] **and René Pernas-Salomón**[2]

[1] Faculty of Mechanical Engineering, Technion–Israel Institute of Technology, Haifa 32000, Israel
[2] Instituto de Física, Benemérita Universidad Autónoma de Puebla, Ciudad Universitaria, Puebla, México

E-mail: meshmuel@tx.technion.ac.il

Received 11 July 2016, revised 16 September 2016
Accepted for publication 11 October 2016
Published 10 November 2016

Abstract

We investigate the effect electrostatically-controlled aperiodicity has on the propagation of flexural waves in two-component elastomeric films. We first determine the static response of the film to a combination of an axial force and voltage over selected segments. Thus, in response to the accumulated charge, the elastomer confined geometrical and physical changes introduce aperiodicity in the film. We then develop the equation governing superposed flexural motions, accounting for the elastomer stiffening and static finite deformation. We adapt a stable matrix method based on this equation to compute the transmission characteristics of the film. Through numerical examples, we show that these characteristics significantly depend on which segments are actuated, i.e., on the resultant aperiodicity. These findings promise a new strategy to control elastic waves.

Keywords: dielectric elastomer, finite deformation, phononic crystal, composite, wave propagation, band gap, localization

(Some figures may appear in colour only in the online journal)

1. Introduction

Periodic heterogeneity of an elastic structure causes a decay of motions at certain frequencies, as they move afar from their source (Sigalas and Economou 1992). These frequencies form gaps in the corresponding frequency spectrum, referred to as elastic *bandgaps* (Kushwaha *et al* 1993); intervals of frequencies outside these bandgaps are called *passbands*, at which waves pass without attenuation. By virtue of this wave suppression, elastic composites has the potential to function as waveguides (Ma *et al* 2013), filter undesired vibrations (Yin *et al* 2015), and reduce noise (Babaee *et al* 2016).

The prohibited frequencies depend on the physical and geometrical properties of the repetitive element constituents. Thus, if the properties of the constituents are susceptible to external loads, the bandgaps of the structure are tunable by such stimuli (Ruzzene and Baz 1999, Bertoldi and Boyce 2008, Degraeve *et al* 2015, Bayat and Gordaninejad 2015). Accordingly, its functionality can be adapted for different transmission purposes, rather than having it fixed from the outset; such a structure is called *active* or *smart.*

Under certain circumstances, a change in the properties of a few sections in the structure will spatially confine motions which would otherwise propagate in the periodic structure (Hodges 1982, Bendiksen 2000). This phenomenon of *mode localization* has recently led to the paradigm of motion manipulation through aperiodic design (see, e.g., Maciá 2012). It follows that localization in smart composites can be employed by introducing aperiodicity through confined activation. The advantage of motion control by mode localization over tuning the band diagram of a smart composite is twofold. First, less power is required to activate part of the structure than to activate the structure in whole. Second, the transmission characteristics change in a more intricate manner when aperiodicity is induced.

The introduction above has set the stage to present the focus of this work—mode localization in *dielectric elastomer* films via controlled aperiodicity. A dielectric elastomer film is actuated by coating its surfaces with compliant electrodes, and subsequently applying voltage (Pelrine *et al* 1998, Liu *et al* 2009, Cohen and deBotton 2014). The ensuing accumulation of charge on the electrodes gives rise to Coulomb forces. Since the film is thin and soft, these forces are

sufficient to contract its thickness, with strains greater than 100% (Pelrine *et al* 2000a). The resultant large deformation modifies the material microstructure through its polymer chains, thereby the film stiffens (Treloar 1975, Gent 1996), and—depending on the particular substance—its permittivity may decrease (Tröls *et al* 2013, Díaz-Calleja and Riande 2013). This actuation principle has been utilized to tune motions through elastomeric tubes (Shmuel and deBotton 2013, Shmuel 2015), membranes (Shmuel *et al* 2012, Zhang *et al* 2015, Jia *et al* 2016) and composites (Yang and Chen 2008, Wu *et al* 2009, Gei *et al* 2011, Shmuel and deBotton 2012, Zhou and Chen 2013, Shmuel 2013); electrostatically controlled aperiodic structures, however, have yet to be exploited.

We propose harnessing electrostatically induced aperiodicity to control mechanical motions in the following system. We consider a film which is made of a periodic repetition of two different incompressible elastomers. First, the film is pre-stretched by application of an axial force, to enhance actuation performance (Kofod 2008, Tröls *et al* 2013). Subsequently, selected segments of the film are subjected to voltage, to break the periodicity of the film in a controlled manner; the resultant static deformation is determined analytically. We then examine the response of the actuated film to incremental flexural excitations. Using a stable matrix method, we compute the transmission characteristics of the film. Through numerical examples, we show that these characteristics significantly depend on the resultant aperiodicity. Thereby, a new strategy to control elastic waves in soft films is demonstrated. Glancing towards possible applications, the envisioned system thus offers a new approach for the locomotion soft robots (Onal and Rus 2013, Sun *et al* 2016), actuation as artificial muscles (Anderson *et al* 2012), energy trapping (Nakamura 1996) and wave focusing (Yi *et al* 2016).

The analysis is delivered as follows. We provide the necessary theory on the mechanics of deformable dielectrics in section 2. Based on this framework, in section 3 we develop the equation governing flexural motions of the finitely deformed two-component film. Section 4 details a stable matrix method to evaluate the corresponding transmission characteristics of the film. The method is utilized in section 5 to study the effect mode localization has on these characteristics, by way of numerical examples. Section 6 concludes the paper, summarizing our main results and observations.

2. Mechanics of deformable dielectrics

This section summarizes the theoretical background required for the sequel. For a comprehensive description of nonlinear electroelasticity, the reader is referred to Dorfmann and Ogden (2005, 2010). (See also Toupin 1963, McMeeking and Landis 2005, deBotton *et al* 2007, Suo *et al* 2008, Castañeda and Siboni 2012, Liu 2013.)

Let $\Omega_0 \subset \mathbb{R}^3$ denote a stress-free configuration of a body made of distinct elastic dielectric phases, and surrounded by vacuum. We label the body points by their position $\mathbf{X}$ in Ω_0, and denote their quasi-static deformation by the continuous function $\boldsymbol{\chi} : \Omega_0 \to \mathbb{R}^3$. The image $\mathbf{x} = \boldsymbol{\chi}(\mathbf{X})$ defines the body current configuration Ω. Let $\mathrm{d}\mathbf{X}$, $\mathrm{d}A$, and $\mathrm{d}V$ respectively denote line, area and volume elements in the vicinity of $\mathbf{X}$; respectively, their counterparts $\mathrm{d}\mathbf{x}$, $\mathrm{d}a$ and $\mathrm{d}v$ in the vicinity of $\mathbf{x}$ are given via

$$\mathrm{d}\mathbf{x} = \mathbf{F}\mathrm{d}\mathbf{X},\ \mathbf{n}\mathrm{d}a = J\mathbf{F}^{-\mathrm{T}}\mathbf{N}\mathrm{d}A,\ \mathrm{d}v = J\mathrm{d}V, \tag{1}$$

where $\mathbf{F} = \nabla_{\mathbf{X}}\boldsymbol{\chi} \equiv \partial\boldsymbol{\chi}/\partial\mathbf{X}$, $J = \det\mathbf{F}$, and $\mathbf{N}$ and $\mathbf{n}$ are the normals to $\mathrm{d}A$ and $\mathrm{d}a$, respectively. If the material is incompressible, the deformation is constrained such that $J = 1$.

The electric field and the electric displacement field in the current configuration are denoted by $\mathbf{e}$ and $\mathbf{d}$, respectively. In absence of body charge, and assuming electromagnetic interactions are negligible, $\mathbf{e}$ and $\mathbf{d}$ satisfy

$$\nabla \cdot \mathbf{d} = 0,\ \nabla \times \mathbf{e} = \mathbf{0}, \tag{2}$$

where $\nabla\cdot$ (resp. $\nabla\times$) is the divergence (resp. curl) operator with respect to $\mathbf{x}$.

In the presence of electric field and/or mechanical loads, the equilibrium equations in Ω can be written in the form

$$\nabla \cdot \boldsymbol{\sigma} = \mathbf{0}, \tag{3}$$

where $\boldsymbol{\sigma}$ is the *total* stress tensor (Dorfmann and Ogden 2005). Note that mechanical body forces were neglected in equation (3).

The formulation of a boundary-value problem is completed with the specification of the following jump conditions. At the interface between a phase a and its neighboring phase b, the conditions are

$$[\![\boldsymbol{\sigma}]\!]\mathbf{n} = \mathbf{0},\quad [\![\mathbf{d}]\!] \cdot \mathbf{n} = 0,\quad [\![\mathbf{e}]\!] \times \mathbf{n} = \mathbf{0}, \tag{4}$$

with $[\![\bullet]\!] \equiv \bullet^{(a)} - \bullet^{(b)}$, and here and throughout this paper, superscript a (resp. b) denotes a quantity in phase a (resp. b). Equation (4) assumes there is no charge between the phases. The jump conditions across the external boundary of the body are

$$(\boldsymbol{\sigma} - \boldsymbol{\sigma}^\star)\mathbf{n} = \mathbf{t}_m,\quad (\mathbf{d} - \mathbf{d}^\star) \cdot \mathbf{n} = -w_e,\quad (\mathbf{e} - \mathbf{e}^\star) \times \mathbf{n} = \mathbf{0}; \tag{5}$$

herein, superscript $\star$ denotes fields outside the body, $\mathbf{t}_m$ is a prescribed mechanical traction, and w_e is the surface charge density, respectively. The *Maxwell* stress outside the body, $\boldsymbol{\sigma}^\star$, is given in terms of $\mathbf{e}^\star$ and the vacuum permittivity ε_0, via

$$\boldsymbol{\sigma}^\star = \varepsilon_0\left[\mathbf{e}^\star \otimes \mathbf{e}^\star - \frac{1}{2}(\mathbf{e}^\star \cdot \mathbf{e}^\star)\mathbf{I}\right]. \tag{6}$$

It is convenient to recast equations (2)–(5), having $\mathbf{X}$ as the independent variable of the *total* first Piola-Kirchhoff $\mathbf{P}$, Lagrangian electric field $\mathbf{E}$, and the Lagrangian electric displacement field $\mathbf{D}$ (see Dorfmann and Ogden 2005).

$$\mathbf{P} = J\boldsymbol{\sigma}\mathbf{F}^{-\mathrm{T}},\ \mathbf{D} = J\mathbf{F}^{-1}\mathbf{d},\ \mathbf{E} = \mathbf{F}^{\mathrm{T}}\mathbf{e}. \tag{7}$$

Adopting the approach of Dorfmann and Ogden (2005), $\mathbf{P}$ and $\mathbf{E}$ are derived from an *augmented* energy density

function, $\Psi(\mathbf{F}, \mathbf{D}, \mathbf{X})$, via

$$\mathbf{P} = \frac{\partial \Psi}{\partial \mathbf{F}} - p_0 \mathbf{F}^{-\mathrm{T}}, \quad \mathbf{E} = \frac{\partial \Psi}{\partial \mathbf{D}}, \tag{8}$$

where p_0 is a Lagrange multiplier, accounting for the incompressibility constraint.

Let Ω' denote a configuration close to Ω, obtained through a time-dependent deformation $\boldsymbol{\chi}'(\mathbf{X}, t)$. Denote by $\dot{\mathbf{P}}$ the difference between and $\mathbf{P}$ and $\mathbf{P}'$—the total Piola-Kirchhoff stress associated with Ω'—such that $\dot{\mathbf{P}} = \mathbf{P}' - \mathbf{P}$. The incremental governing equations can be written compactly using Ω and $\mathbf{x}$ instead of Ω_0 and $\mathbf{X}$ as the *updated* reference quantities, as follows. The increment $\dot{\mathbf{P}}$ is updated to $\boldsymbol{\Sigma} = J^{-1}\dot{\mathbf{P}}\mathbf{F}^{\mathrm{T}}$, which satisfies

$$\nabla \cdot \boldsymbol{\Sigma} = \rho \dot{\mathbf{x}}_{,tt}, \tag{9}$$

where ρ is the mass density, and $\dot{\mathbf{x}}(\mathbf{x}, t) \coloneqq \boldsymbol{\chi}'(\boldsymbol{\chi}^{-1}(\mathbf{x}), t) - \mathbf{x}$. In case the electric perturbations accompanying $\boldsymbol{\chi}'$ are negligible, the stress measure $\boldsymbol{\Sigma}$ has the linear approximation

$$\boldsymbol{\Sigma} = \mathscr{C}\mathbf{h} + p_0 \mathbf{h}^{\mathrm{T}} - \dot{p}_0 \mathbf{I}, \tag{10}$$

where $\mathscr{C}_{ijkl} = J^{-1}F_{j\alpha}\frac{\partial^2 \Psi}{\partial F_{i\alpha}\partial F_{k\beta}}F_{l\beta}$, and $\mathbf{h} = \nabla \dot{\mathbf{x}}$. Note that incompressibility requires

$$\mathrm{tr}\mathbf{h} = 0. \tag{11}$$

When $\boldsymbol{\sigma}^\star = \mathbf{0}$ and the prescribed loads are independent of the deformation, the condition for $\boldsymbol{\Sigma}$ across the outer boundary reads

$$\boldsymbol{\Sigma}\mathbf{n} = \mathbf{0}. \tag{12}$$

3. Flexural motions of a two-component thin soft dielectric film

Consider a thin film made out of M repetitions of a unit-cell. The unit-cell comprises two incompressible soft dielectrics, referred to as phase a and phase b. At the reference state, the phases have an equal thickness, $H = H^{(a)} = H^{(b)}$, and an equal width, $B = B^{(a)} = B^{(b)}$. The length of the unit-cell, L, is the sum of the length of each phase, i.e., $L = L^{(a)} + L^{(b)}$ (see figure 1(a)). Note that $L^{(a)}$ may differ from $L^{(b)}$.

The constitutive response of each component is described by an energy function of $I_1 = \mathrm{tr}\mathbf{F}^{\mathrm{T}}\mathbf{F}$, $I_4 = \mathbf{D}\cdot\mathbf{D}$, $I_5 = \mathbf{FD}\cdot\mathbf{FD}$, and $I_6 = \mathbf{D}\cdot(\mathbf{F}^{\mathrm{T}}\mathbf{F})^2\mathbf{D}$, in the form

$$\Psi^{(p)} = W^{(p)}(I_1) + \frac{1}{2\varepsilon^{(p)}}(\gamma_0^{(p)} I_4 + \gamma_1^{(p)} I_5 + \gamma_2^{(p)} I_6). \tag{13}$$

Herein, $W^{(p)}(I_1)$ is a nonlinear function of I_1, and $\gamma_0^{(p)}$, $\gamma_1^{(p)}$ and $\gamma_2^{(p)}$ are material constants aimed at capturing a deformation-dependent material permittivity (Gei *et al* 2014, Cohen *et al* 2016); with the constraint $\sum_{i=1}^{3}\gamma_i^{(p)} = 1$, the constant $\varepsilon^{(p)}$ is identified as the dielectric constant in the limit of small strains.

We determine first the deformation of the film when subjected to an axial force N, while its top and bottom surfaces are free of mechanical traction. The boundaries normal to the width are subjected to sliding conditions, thereby approximating a state of plane-strain. On account of the translational symmetry in each phase, we postulate a resultant piecewise homogeneous deformation. Note that the continuity of the deformation implies that inhomogeneous deformations evolve near the interfaces between the phases, transitioning between the homogeneous deformations of each phase. To describe the homogeneous deformation $\mathbf{F}^{(p)}$ in each phase, we employ a Cartesian system whose origin at the centroid of the film and the coordinates X_1, X_2 and X_3 are along the length, the thickness and the width of the film, respectively. In these coordinates, the matrix representation of $\mathbf{F}^{(p)}$ is

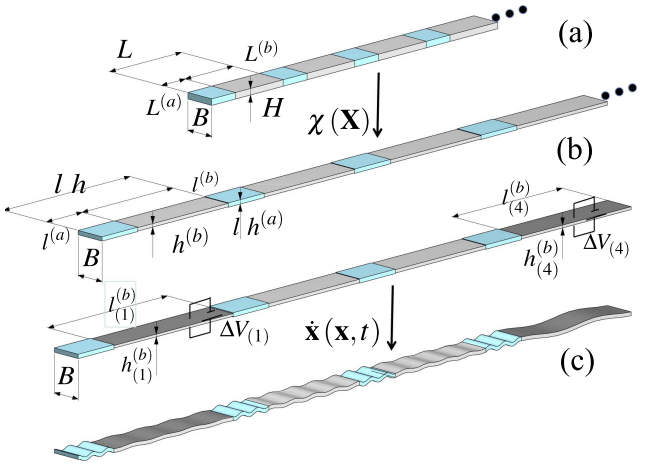

Figure 1. An illustration of four cells in a soft dielectric film (a) at the reference state; (b) deformed by an axial tension, while phase (b) in cells 1 and 4 is subjected to $\Delta V_{(1)}$ and $\Delta V_{(4)}$, respectively; (c) when incremental flexural motions are superposed on top of the static finite deformation.

$$\mathsf{F}^{(p)} = \mathrm{diag}[\lambda^{(p)}, 1/\lambda^{(p)}, 1]. \tag{14}$$

Accordingly, the resultant length and thickness of each phase are $l^{(p)} = \lambda^{(p)}L^{(p)}$ and $h^{(p)} = H/\lambda^{(p)}$, respectively (see figure 1(b)). The stretches $\lambda^{(p)}$ are determined as functions of the axial force N from the following jump and boundary conditions. The traction-free conditions at the upper and lower surfaces provide

$$\sigma_{22}^{(p)} = 2\frac{\Psi_{,1}^{(p)}}{\lambda^{(p)^2}} - p_0^{(p)} = 0, \tag{15}$$

where $\Psi_{,i}^{(p)} = \partial\Psi^{(p)}/\partial I_i$, from which $p_0^{(p)}$ are calculated. Note that equation (15) uses the fact that $\boldsymbol{\sigma}^\star = \mathbf{0}$, since $\mathbf{e}^\star$ vanishes on account of the symmetry of the problem with respect to the mid-plane. To equilibrate N, the axial stress component must satisfy

$$\frac{N}{B} = \sigma_{11}^{(p)}\frac{H}{\lambda^{(p)}} = (2\Psi_{,1}^{(p)}\lambda^{(p)^2} - p_0^{(p)})\frac{H}{\lambda^{(p)}}$$
$$= 2\Psi_{,1}^{(p)}\left(\lambda^{(p)^2} - \frac{1}{\lambda^{(p)^2}}\right)\frac{H}{\lambda^{(p)}}. \tag{16}$$

Equation (16) delivers the nonlinear relation between $\lambda^{(p)}$ and N, for any constitutive model $\Psi^{(p)}$ which depends on I_1.

Consider next an electrostatic actuation of *selected* phases in the film, in addition to the axial force. Specifically, phase p in a selected cell n is subjected to a voltage $\Delta V_{(n)}$; throughout the sequel, subscript (n) denotes the value of the quantity in cell n. Such a voltage difference is established by coating the upper and lower surfaces of the phase with compliant electrodes, and connecting them to a power source. The resultant electric field in the selected phase has along the thickness the component

$$e_{2(n)}^{(p)} = \frac{\Delta V_{(n)}}{H^{(p)}/\lambda_{(n)}^{(p)}}. \tag{17}$$

In turn, the expression for $\sigma_{22(n)}^{(p)}$ becomes

$$\sigma_{22(n)}^{(p)} = 2\frac{\Psi_{,1}^{(p)}}{\lambda_{(n)}^{(p)^2}} - p_{0(n)}^{(p)} + \frac{\gamma_1^{(p)} + 2\lambda^{(p)^{-2}}\gamma_2^{(p)}}{(\gamma_0^{(p)}\lambda_{(n)}^{(p)^2} + \gamma_1^{(p)} + \gamma_2^{(p)}\lambda_{(n)}^{(p)^{-2}})^2}\varepsilon^{(p)}\left(\frac{\Delta V_{(n)}}{H/\lambda_{(n)}^{(p)}}\right)^2 = 0. \tag{18}$$

The procedure to calculate $\lambda_{(n)}^{(p)}$ is similar to the calculation of $\lambda^{(p)}$ in the absence of electric loads. Thus, we determine $p_{0(n)}^{(p)}$ from equation (18), and substitute it into equation (16); the solution of the resultant nonlinear equation provides $\lambda_{(n)}^{(p)}$ as a function of N and $\Delta V_{(n)}$, for any constitutive model in the form of equation (13).

We emphasize that the scheme above allows to choose the spacing between the actuated phases. Thereby, with a choice of irregular spacing between actuated phases, it provides a mechanism for controlled aperiodicity. In the sequel, we demonstrate how such aperiodicity is exploited to manipulate incremental flexural motions of the deformed film. The first step towards this end is to derive the corresponding governing equation. On account of the slenderness of the film, we employ a structural approach, through the calculation of the relation between the bending moment and the deflection. Essentially, we derive a counterpart of an Euler–Bernoulli model, accounting for the large static deformation and the material nonlinearity. We use the configuration Ω as the updated reference configuration, for which the tensor that relates an area element $\mathrm{d}a \in \Omega$ to the traction $\mathbf{t}'$ acting on a area element $\mathrm{d}a'$ in Ω' is

$$\mathbf{t}'\mathrm{d}a' = \mathbf{P}'\mathbf{N}\mathrm{d}A = \mathbf{P}'\mathbf{F}^{\mathrm{T}}\mathbf{n}\mathrm{d}a. \tag{19}$$

Temporarily suppressing phase and cell notation, we find that the bending moment $\mathbf{m}$ equals

$$\begin{aligned}\mathbf{m} &= \int_{\partial\Omega} \mathbf{x}\times\mathbf{P}'\mathbf{F}^{\mathrm{T}}\mathbf{n}\mathrm{d}a = \int_{\partial\Omega} x_2\mathbf{i}_2\times(\mathbf{P}+\dot{\mathbf{P}})\mathbf{F}^{\mathrm{T}}\mathbf{n}\mathrm{d}a \\ &= \int_{\partial\Omega} x_2\mathbf{i}_2\times\dot{\mathbf{P}}\mathbf{F}^{\mathrm{T}}\mathbf{n}\mathrm{d}a = \int_{\partial\Omega} x_2\mathbf{i}_2\times\boldsymbol{\Sigma}\mathbf{n}\mathrm{d}a \\ &= \int_{\partial\Omega} x_2\mathbf{i}_2\times\Sigma_{11}\mathbf{i}_1\mathrm{d}a = -B\int_{-h/2}^{h/2}\Sigma_{11}x_2\mathrm{d}x_2\mathbf{i}_3;\end{aligned} \tag{20}$$

herein, $\mathbf{i}_1$, $\mathbf{i}_2$ and $\mathbf{i}_3$ are unit vectors along the coordinates x_1, x_2 and x_3, respectively, and $\partial\Omega$ is the cross section of the film at Ω, whose normal is $\mathbf{i}_1$. Equation (20) tacitly assumes that $\dot{\mathbf{x}}$ is small in a way that $\mathbf{x} \cong (\boldsymbol{\chi}' \circ \boldsymbol{\chi}^{-1})(\mathbf{x})$ for the purpose of calculating $\mathbf{m}$. In passing between the rows in equation (20), the product $\int_{\partial\Omega} x_2\mathbf{i}_2\times\mathbf{P}\mathbf{F}^{\mathrm{T}}\mathbf{n}\mathrm{d}a$ vanishes since P_{11} is a constant. The component Σ_{11} is

$$\begin{aligned}\Sigma_{11} &= (\mathscr{C}_{1111}+p_0)h_{11} + \mathscr{C}_{1122}h_{22} - \dot{p}_0 \\ &= (\mathscr{C}_{1111}+p_0-\mathscr{C}_{1122})h_{11} - \dot{p}_0,\end{aligned} \tag{21}$$

where the incompressibility constraint $h_{11}+h_{22}=0$ was used, and

$$\mathscr{C}_{1111} = 4\Psi_{,11}\lambda^4 + 2\Psi_{,1}\lambda^2,\ \mathscr{C}_{1122} = 4\Psi_{,11}. \tag{22}$$

Based on standard analysis, h_{11} is related to the deflection via

$$h_{11} \equiv \dot{x}_{1,1} = -x_2\frac{\dot{x}_{2,11}}{\sqrt{1+\dot{x}_{2,1}^2}} \cong -x_2\dot{x}_{2,11}, \tag{23}$$

where the last transition relies on the assumption that the superposed strains are small. Substituting equations (21) and (23) back into equation (20) yields the the relation between the moment and the deflection

$$\mathbf{m} = \dot{x}_{2,11}(\mathscr{C}_{1111}+p_0-\mathscr{C}_{1122})I\mathbf{i}_3 + B\int_{-h/2}^{h/2}\dot{p}_0x_2\mathrm{d}x_2\mathbf{i}_3, \tag{24}$$

where $I \coloneqq B\int_{-h/2}^{h/2}x_2^2\mathrm{d}x_2$. Since the film is very thin, we have assumed that $\dot{x}_{2,11}$ is independent of x_2. Equation (24) depends on the value of $\dot{p}_0$, which is calculated through Σ_{22} as follows. The incremental traction is zero at the top and bottom surfaces, therefore at these boundaries Σ_{22} vanishes. Further, it cannot vary much in-between, since the film is thin. Accordingly, Σ_{22} is approximately zero throughout the thickness, i.e.,

$$\Sigma_{22} = \mathscr{C}_{2211}h_{11} + \mathscr{C}_{2222}h_{22} + p_0h_{22} - \dot{p}_0 = 0, \tag{25}$$

with

$$\mathscr{C}_{2211} = 4\Psi_{,11},\ \mathscr{C}_{2222} = 4\Psi_{,11}\lambda^{-4} + \Psi_{,1}\lambda^{-2} + \frac{\gamma_1+2\gamma_2+4}{(\lambda^2\gamma_0+\gamma_1+\lambda^{-2}\gamma_2)^2}\varepsilon\left(\frac{\Delta V}{H/\lambda}\right)^2. \tag{26}$$

The value of $\dot{p}_0$ is obtained from (25), and substituted into equation (24). The final result reads

$$\mathbf{m} = \dot{x}_{2,11}EI\mathbf{i}_3, \tag{27}$$

where $E \coloneqq \mathscr{C}_{1111}+\mathscr{C}_{2222}+2p_0-2\mathscr{C}_{1122}$. We dwell momentarily on the value of E. It is clear from equations (24) and (27) that the instantaneous stiffness E relating $\mathbf{m}$ and $\dot{x}_{2,11}$ depends on p_0 and $\dot{p}_0$. In turn, these Lagrange multipliers depend on the boundary conditions. Specifically, when the top and bottom faces are free of traction throughout the finite and incremental deformation, the boundary conditions (15) and (25) are used. The resultant expression for E agrees with the expression used by Gei *et al* (2011) and the references therein, who ignored the effect incompressibility has on the instantaneous elasticities through p_0 and $\dot{p}_0$. However, when a voltage is applied, the condition (15) is replaced with equation (18), and the expression for the instantaneous

stiffness E differs from the former case. Thus, we emphasize that in any case at which the boundaries are not free of traction throughout the finite and the incremental deformations, the Lagrange multipliers must be accounted for when calculating the instantaneous elasticities.

Returning to the derivation of the governing equation, we apply the balance of linear momentum to a differential element of the film, in conjunction with relation (27). Similarly to the derivations in the Euler–Bernoulli theory (Graff 1975), we find that

$$-EI\dot{x}_{2,1111} + N\dot{x}_{2,11} = \rho a\dot{x}_{2,tt}. \tag{28}$$

Equation (28) is solved with

$$\dot{x}_2 = (C_1^+ e^{i\alpha x_1} + C_2^+ e^{i\beta x_1} + C_1^- e^{-i\alpha x_1} + C_2^- e^{-i\beta x_1})e^{-i\omega t}, \tag{29}$$

where

$$\alpha = \sqrt{\frac{-N + \sqrt{N^2 + 4EI\rho a\omega^2}}{2EI}},$$
$$\beta = i\sqrt{\frac{N + \sqrt{N^2 + 4EI\rho a\omega^2}}{2EI}}, \tag{30}$$

and ω is the angular frequency. We identify C_1^+ and C_2^+ (resp. C_1^- and C_2^-) as the amplitudes of waves propagating to the right (resp. left). We recall that E, I and a are phase-wise constants, which depend on the axial force N, the applied voltage $\Delta V_{(n)}$, and the constitutive law $\Psi^{(p)}$. We thus emphasize that each phase is associated with different values of E, I, ρ, α, β, C_1^+, C_2^+, C_1^- and C_2^-. The outstanding issue, addressed next, is to determine the characteristics of the propagation in the *heterogeneous* film.

4. A stable matrix formulation for propagation analysis

The mechanical state at each section of the film is determined by the deflection, angle of rotation, shear force, and the bending moment at that section. To introduce how these vary along the film, we consider first a homogeneous film, for which it is convenient to gather these quantities into a so-called *state vector* $\mathbf{s}(x_1)$. In terms of the matrix $\mathsf{Q}_h(x_1)$ and the coefficient vector $\mathbf{c}$

$$\mathsf{Q}_h(x_1) = \begin{bmatrix} e^{i\alpha x_1} & e^{i\beta x_1} & e^{-i\alpha x_1} & e^{-i\beta x_1} \\ i\alpha e^{i\alpha x_1} & i\beta e^{i\beta x_1} & -i\alpha e^{-i\alpha x_1} & -i\beta e^{-i\beta x_1} \\ -EI\alpha^2 e^{i\alpha x_1} & -EI\beta^2 e^{i\beta x_1} & -EI\alpha^2 e^{-i\alpha x_1} & -EI\beta^2 e^{-i\beta x_1} \\ iEI\alpha^3 e^{i\alpha x_1} & iEI\beta^3 e^{i\beta x_1} & -iEI\alpha^3 e^{-i\alpha x_1} & -iEI\beta^3 e^{-i\beta x_1} \end{bmatrix},$$
$$\mathbf{c} = \begin{Bmatrix} C_1^+ \\ C_2^+ \\ C_1^- \\ C_2^- \end{Bmatrix}, \tag{31}$$

the state vector is

$$\mathbf{s}(x_1) = \begin{Bmatrix} \dot{x}_2 \\ \dot{x}_{2,1} \\ EI\dot{x}_{2,11} \\ -EI\dot{x}_{2,111} \end{Bmatrix} = \mathsf{Q}_h(x_1)\cdot\mathbf{c}. \tag{32}$$

The state vectors at the ends of a homogeneous film of length l are related via

$$\mathbf{s}(l) = \mathsf{T}\cdot\mathbf{s}(0), \tag{33}$$

where $\mathsf{T} \coloneqq \mathsf{Q}_h(l)\mathsf{Q}_h^{-1}(0)$ is called the *transfer matrix* (see Carta and Brun 2015, and the references therein).

For the addressed heterogeneous film, expressions (31)–(33) depend on the phase and cell. We can relate their corresponding state vectors at interfaces between different phases on account of the continuity requirements. These conditions write

$$\mathbf{s}_{(n)}^{(a)} = \mathbf{s}_{(n)}^{(b)} \text{ at } \partial\Omega_{(n)},\ \mathbf{s}_{(n)}^{(b)} = \mathbf{s}_{(n+1)}^{(a)} \text{ at } \partial\Omega_{(n,n+1)}, \tag{34}$$

where $\partial\Omega_{(n)}$ (resp. $\partial\Omega_{(n,n+1)}$) is the interface between phases a and b in cell n (resp. between cells n and $n+1$). Equation (34) tacitly assumes that the transition between the different deformations of each phase is sufficiently small. A recursive application of equation (34) provides the relation between the state vectors at the ends of the whole film, namely

$$\mathbf{s}_{(M)}^{(b)}(l_{\text{tot}}) = \mathsf{T}_{\text{tot}}\mathbf{s}_{(1)}^{(a)}(0), \tag{35}$$

where $\mathsf{T}_{\text{tot}} \coloneqq \prod_{n=M}^{1}\mathsf{T}_{(n)}$, $\mathsf{T}_{(n)} \coloneqq \mathsf{T}_{(n)}^{(b)}\mathsf{T}_{(n)}^{(a)}$, and l_{tot} is the total length of the film. The *total transfer matrix* T_{tot} encompasses all the information on the wave propagation characteristics through the film. However, T_{tot} has inherent numerical instabilities that prevent its practical computation, and in turn, the characteristics of the propagation. To explain the source of these numerical issues, consider an arbitrary transfer matrix of a certain cell. Waves propagating within are associated with real eigenvalues, whose corresponding exponents magnitude is bounded by 1; evanescent modes are associated with imaginary eigenvalues, whose corresponding exponents magnitude grows indefinitely as function of the product of the frequency and the spatial coordinate. Thereby, two numerical problems follow. (i) The calculation of T_{tot} involves arithmetic operations between numbers which are different by hundreds of orders; this results with numerical errors and an ill-conditioned matrix. (ii) Beyond a certain value, the magnitude of exponents exceeds machine representation capability, and an arithmetic overflow occurs. A rigorous analysis of the numerical instability and its resolution of this matrix approach for the Sturm-Liouville problem are detailed in Rokhlin and Wang (2002), Tan (2006), Pernas-Salomón *et al* (2015), Pérez-Álvarez *et al* (2015), and the references therein. A direct implementation of the methods reported in the references above is not feasible, as the numerical instability is significantly more severe in matrices associated with differential equations of the kind in equation (28), due to the following reasons. (i) The eigenvalues appear up to their third power in the transfer matrix, thereby increasing its condition

number. By contrast, in the transfer matrix for the Sturm-Liouville equation, only the first and second powers appear. (ii) The axial pre-stress brings with numerical instabilities and overflow also at low frequencies. This is evident from the expressions in equation (30), whose exponents have real arguments in the transfer matrix even when ω vanishes. The problem stems from the second derivative of $\dot{x}_2$ in the fourth order differential equation (28), introduced by the pre-stress.

To tackle these difficulties, we adapt to our settings a scattering matrix derived from a Hybrid matrix (Tan 2006, Pernas-Salomón *et al* 2015), as follows. First, we define Q by multiplying the second, third and fourth rows of Q_h by the factors $\beta^{(a)^{-1}}$, $\beta^{(a)^{-2}}/E^{(a)}I^{(a)}$ and $\beta^{(a)^{-3}}/E^{(a)}I^{(a)}$, respectively. Accordingly, we define a modified state vector

$$\mathbf{s}_{\mathrm{m}}(x_1)=\begin{Bmatrix}\dot{x}_2\\ \dot{x}_{2,1}\beta^{(a)^{-1}}\\ \frac{E(x_1)I(x_1)}{E^{(a)}I^{(a)}}\dot{x}_{2,11}\beta^{(a)^{-2}}\\ -\frac{E(x_1)I(x_1)}{E^{(a)}I^{(a)}}\dot{x}_{2,111}\beta^{(a)^{-3}}\end{Bmatrix}, \tag{36}$$

and denote its first two components by $\mathbf{s}_{\mathrm{d}}(x_1)$, and his last two components by $\mathbf{s}_{\mathrm{f}}(x_1)$. These can be written in terms of the sub-blocks of the modified matrix Q, such that

$$\begin{aligned}\mathbf{s}_{\mathrm{d}}(x_1)&=\mathsf{Q}_{\mathrm{d}}^{+}(x_1)\cdot\mathbf{c}^{+}+\mathsf{Q}_{\mathrm{d}}^{-}(x_1)\cdot\mathbf{c}^{-},\\ \mathbf{s}_{\mathrm{f}}(x_1)&=\mathsf{Q}_{\mathrm{f}}^{+}(x_1)\cdot\mathbf{c}^{+}+\mathsf{Q}_{\mathrm{f}}^{-}(x_1)\cdot\mathbf{c}^{-},\end{aligned} \tag{37}$$

where

$$\begin{aligned}&\mathbf{c}^{+}=\begin{Bmatrix}C_1^{+}\\ C_2^{+}\end{Bmatrix},\ \mathbf{c}^{-}=\begin{Bmatrix}C_1^{-}\\ C_2^{-}\end{Bmatrix},\\ &\mathsf{Q}_{\mathrm{d}}^{+}(x_1)=\mathsf{Q}_{11}(x_1)\\ &\quad=\begin{bmatrix}e^{i\alpha x_1} & e^{i\beta x_1}\\ i\frac{\alpha}{\beta^{(a)}}e^{i\alpha x_1} & i\frac{\beta}{\beta^{(a)}}e^{i\beta x_1}\end{bmatrix},\\ &\mathsf{Q}_{\mathrm{d}}^{-}(x_1)=\mathsf{Q}_{12}(x_1)\\ &\quad=\begin{bmatrix}e^{-i\alpha x_1} & e^{-i\beta x_1}\\ -i\frac{\alpha}{\beta^{(a)}}e^{i\alpha x_1} & -i\frac{\beta}{\beta^{(a)}}e^{i\beta x_1}\end{bmatrix},\\ &\mathsf{Q}_{\mathrm{f}}^{+}(x_1)=\mathsf{Q}_{21}(x_1)\\ &\quad=\begin{bmatrix}-\frac{EI}{E^{(a)}I^{(a)}}\left(\frac{\alpha}{\beta^{(a)}}\right)^2e^{i\alpha x_1} & -\frac{EI}{E^{(a)}I^{(a)}}\left(\frac{\beta}{\beta^{(a)}}\right)^2e^{i\beta x_1}\\ i\frac{EI}{E^{(a)}I^{(a)}}\left(\frac{\alpha}{\beta^{(a)}}\right)^3e^{i\alpha x_1} & i\frac{EI}{E^{(a)}I^{(a)}}\left(\frac{\beta}{\beta^{(a)}}\right)^3e^{i\beta x_1}\end{bmatrix},\\ &\mathsf{Q}_{\mathrm{f}}^{-}(x_1)=\mathsf{Q}_{22}(x_1)\\ &\quad=\begin{bmatrix}-\frac{EI}{E^{(a)}I^{(a)}}\left(\frac{\alpha}{\beta^{(a)}}\right)^2e^{-i\alpha x_1} & -\frac{EI}{E^{(a)}I^{(a)}}\left(\frac{\beta}{\beta^{(a)}}\right)^2e^{-i\beta x_1}\\ -i\frac{EI}{E^{(a)}I^{(a)}}\left(\frac{\alpha}{\beta^{(a)}}\right)^3e^{-i\alpha x_1} & -i\frac{EI}{E^{(a)}I^{(a)}}\left(\frac{\beta}{\beta^{(a)}}\right)^3e^{-i\beta x_1}\end{bmatrix}.\end{aligned} \tag{38}$$

herein, Q_{11}, Q_{12}, Q_{21} and Q_{22} denote the the top right, top left, bottom right, and bottom left 2×2 sub-blocks of the modified Q. We emphasize that E, I, α and β in equation (38) depend on the cell and phase at x_1. Utilizing sub-blocks of a transfer matrix based Q, we compose the cell modified hybrid matrix $\mathsf{H}_{(n)}$, which avoids the aforementioned numerical instabilities, and reads

$$\mathsf{H}_{(n)}=\begin{bmatrix}-\mathsf{T}_{(n)11}^{-1}\cdot\mathsf{T}_{(n)12} & \mathsf{T}_{(n)11}^{-1}\\ \mathsf{T}_{(n)22}-\mathsf{T}_{(n)21}\cdot\mathsf{T}_{(n)11}^{-1}\cdot\mathsf{T}_{(n)12} & \mathsf{T}_{(n)21}\cdot\mathsf{T}_{(n)11}^{-1}\end{bmatrix}; \tag{39}$$

here again, subscripts without brackets refer to the corresponding sub-blocks of the matrix, as defined above for Q. The hybrid matrix of a single cell, whose ends are at $\tilde{x}_1$ and $\tilde{x}_1+l_{(n)}$, relates between the following quantities

$$\begin{aligned}&\begin{Bmatrix}\dot{x}_2(\tilde{x}_1)\\ \beta^{(a)^{-1}}\dot{x}_{2,1}(\tilde{x}_1)\\ \frac{EI}{E^{(a)}I^{(a)}}\beta^{(a)^{-2}}\dot{x}_{2,11}(\tilde{x}_1+l_{(n)})\\ -\frac{EI}{E^{(a)}I^{(a)}}\beta^{(a)^{-3}}\dot{x}_{2,111}(\tilde{x}_1+l_{(n)})\end{Bmatrix}\\ &\quad=\mathsf{H}_{(n)}\cdot\begin{Bmatrix}\frac{EI}{E^{(a)}I^{(a)}}\beta^{(a)^{-2}}\dot{x}_{2,11}(\tilde{x}_1)\\ -\frac{EI}{E^{(a)}I^{(a)}}\beta^{(a)^{-3}}\dot{x}_{2,111}(\tilde{x}_1)\\ \dot{x}_2(\tilde{x}_1+l_{(n)})\\ \beta^{(a)^{-1}}\dot{x}_{2,1}(\tilde{x}_1+l_{(n)})\end{Bmatrix}.\end{aligned} \tag{40}$$

Recursively, the total hybrid matrix of a stack comprising n cells, $\mathsf{H}_{(1,n)}$, is defined in terms of the total hybrid matrix of the first $n-1$ cells, $\mathsf{H}_{(1,n-1)}$, and the hybrid matrix of the nth cell, $\mathsf{H}_{(n)}$, as follows

$$\begin{aligned}\mathsf{H}_{22(1,n)}&=\mathsf{H}_{22(n)}+\mathsf{H}_{21(n)}\cdot[\mathsf{I}_2-\mathsf{H}_{22(1,n-1)}\cdot\mathsf{H}_{11(n)}]^{-1}\\ &\quad\cdot\mathsf{H}_{22(1,n-1)}\cdot\mathsf{H}_{12(n)},\\ \mathsf{H}_{21(1,n)}&=\mathsf{H}_{21(n)}\cdot[\mathsf{I}_2-\mathsf{H}_{22(1,n-1)}\cdot\mathsf{H}_{11(n)}]^{-1}\cdot\mathsf{H}_{21(1,n-1)},\\ \mathsf{H}_{12(1,n)}&=\mathsf{H}_{12(1,n-1)}\cdot\mathsf{H}_{12(n)}+\mathsf{H}_{12(1,n-1)}\cdot\mathsf{H}_{11(n)}\\ &\quad\cdot[\mathsf{I}_2-\mathsf{H}_{22(1,n-1)}\cdot\mathsf{H}_{11(n)}]^{-1}\cdot\mathsf{H}_{22(1,n-1)}\cdot\mathsf{H}_{12(n)},\\ \mathsf{H}_{11(1,n)}&=\mathsf{H}_{11(1,n-1)}+\mathsf{H}_{12(1,n-1)}\cdot\mathsf{H}_{11(n)}\\ &\quad\cdot[\mathsf{I}_2-\mathsf{H}_{22(1,n-1)}\cdot\mathsf{H}_{11(n)}]^{-1}\cdot\mathsf{H}_{21(1,n-1)}.\end{aligned} \tag{41}$$

Finally, we compose the scattering matrix $\mathsf{S}_{(0,M+1)}$, relating the amplitude of waves at the ends of the film (Ko and Sambles 1988, Pérez-Álvarez and García-Moliner 2004)

$$\begin{Bmatrix}\mathbf{c}_{(0)}^{-}\\ \mathbf{c}_{(M+1)}^{+}\end{Bmatrix}=\mathsf{S}_{(0,M+1)}\cdot\begin{Bmatrix}\mathbf{c}_{(0)}^{+}\\ \mathbf{c}_{(M+1)}^{-}\end{Bmatrix}, \tag{42}$$

where subscripts (0) and $(M+1)$ denote the coefficients in the domains preceding and following the film, respectively. The matrix is defined in terms of $\mathsf{H}_{(1,M)}$ and Q, as

$$\begin{aligned}\mathsf{S}_{(0,M+1)}=&\left[\begin{bmatrix}\mathsf{Q}_{\mathrm{d}(0)}^{-} & 0_2\\ 0_2 & \mathsf{Q}_{\mathrm{f}(M)}^{+}\end{bmatrix}-\mathsf{H}_{(1,M)}\cdot\begin{bmatrix}\mathsf{Q}_{\mathrm{f}(0)}^{-} & 0_2\\ 0_2 & \mathsf{Q}_{\mathrm{d}(M)}^{+}\end{bmatrix}\right]^{-1}\\ &\cdot\left[\mathsf{H}_{(1,M)}\cdot\begin{bmatrix}\mathsf{Q}_{\mathrm{f}(0)}^{+} & 0_2\\ 0_2 & \mathsf{Q}_{\mathrm{d}(M)}^{-}\end{bmatrix}-\begin{bmatrix}\mathsf{Q}_{\mathrm{d}(0)}^{+} & 0_2\\ 0_2 & \mathsf{Q}_{\mathrm{f}(M)}^{-}\end{bmatrix}\right],\end{aligned} \tag{43}$$

where 0_2 denotes the 2×2 null matrix. We clarify that $\mathsf{Q}_{\mathrm{d}(0)}^{-}$, $\mathsf{Q}_{\mathrm{d}(0)}^{+}$, $\mathsf{Q}_{\mathrm{f}(0)}^{-}$ and $\mathsf{Q}_{\mathrm{f}(0)}^{+}$ are derived from the matrix Q of the domain (0) preceding the film, at the interface. Similarly, $\mathsf{Q}_{\mathrm{d}(M)}^{-}$, $\mathsf{Q}_{\mathrm{d}(M)}^{+}$, $\mathsf{Q}_{\mathrm{f}(M)}^{-}$ and $\mathsf{Q}_{\mathrm{f}(M)}^{+}$ are derived from the matrix Q of the domain $(M+1)$ following the film, at the interface (see

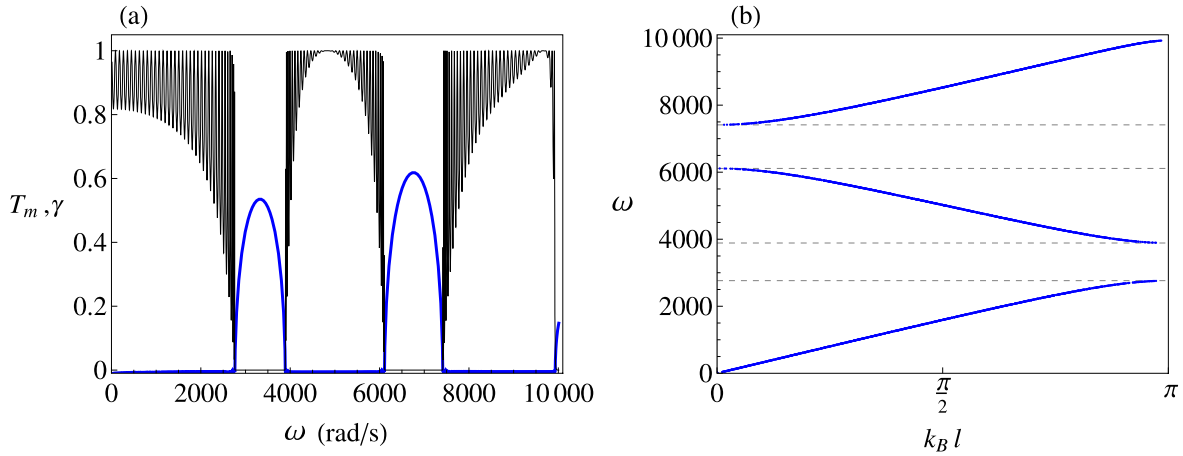

Figure 2. (a) The square of the transmission coefficient, T_m (black curve), and the localization factor γ (blue curve) of a pre-stressed film made of 36 unit cells, as functions of the frequency. (b) The eigenfrequencies of the periodic film as functions of the Bloch parameter k_B.

Pernas-Salomón *et al* 2015, for more details). In the numerical examples to follow, these domains were chosen as phase *a*. The sub-matrices of S are directly related to the reflection and transmission amplitudes in the following two practical scenarios (Pérez-Álvarez and García-Moliner 2004). When only an incident wave from the left is excited, such that $\mathbf{c}^{-}_{(M+1)} = 0$, we have that $\mathsf{S}_{(0,M+1)11}$ and $\mathsf{S}_{(0,M+1)21}$ are the reflection and transmission amplitudes of the reflected wave $\mathbf{c}^{-}_{(0)}$, and the transmitted wave $\mathbf{c}^{+}_{(M+1)}$, respectively. Similarly, when an incident wave arrives from the right while $\mathbf{c}^{+}_{(0)} = 0$, we have that $\mathsf{S}_{(0,M+1)12}$ and $\mathsf{S}_{(0,M+1)22}$ are the transmission and reflection amplitudes of the transmitted wave $\mathbf{c}^{+}_{(M+1)}$, and the reflected wave $\mathbf{c}^{-}_{(0)}$, respectively. In the sequel, we will evaluate the square of the transmission coefficient for an incident wave from the left, given by

$$T_m = \left| \frac{C^{+}_{1(M+1)}}{C^{+}_{1(0)}} \right|^2 = \left| \{1 \;\; 0\} \cdot \mathsf{S}_{(0,M+1)21} \cdot \begin{Bmatrix} 1 \\ 0 \end{Bmatrix} \right|^2 . \quad (44)$$

An additional measure of the transmission characteristics of a heterogeneous medium is the localization factor γ, which quantifies the asymptotic decay of a wave vector which carries energy the farthest. It is calculated as (Kissel 1991)

$$\gamma = -\lim_{M\to\infty} \frac{1}{M} \ln \|\mathsf{S}_{(0,M+1)12}\|_{\max}, \quad (45)$$

where $\|\bullet\|_{\max}$ is the max norm of a matrix, yielding the maximal absolute value over all the components of the matrix. The transmission coefficient and the localization factor are complementary quantities; when T_m vanishes, γ is to be positive, and vice versa—when $\gamma = 0$, T_m is to be greater than zero.

In the subsequent section, we calculate T_m and γ for various examples. Note that γ is defined through the scattering matrix of a structure with an infinite number of cells ($M \to \infty$). Its practical calculation requires employing a truncated number of cells, large enough for γ to converge. In our investigation, different examples required different number of cells for converges, varying between $M = 450$ to $M = 1000$. The augmented film was constructed as follows. When the film has a periodic pattern, its augmentation follows the same periodicity; when the actuation of the phases follows the Fibonacci sequence, the extended film was constructed according to the Fibonacci rule; when the actuation introduces aperiodicity without order, each cell was replaced with a stack of cells, such that the ratio between the actuated cells and the cells that are not actuated is kept.

5. Numerical investigation

The ability to manipulate flexural motions of an elastomeric film through electrostatically induced aperiodicity is demonstrated next, by way of numerical examples. Specifically, we consider a film made out of 36 unit cells pre-stressed by an axial force of 0.75N, and evaluate its transmission characteristics when different arrangements of phases are actuated at different voltages. The geometry of the unit cell is

$$H = 100\ \mu\text{m},\ B = 1\ \text{cm},\ L^{(a)} = 0.5\ \text{cm},\ L^{(b)} = 1\ \text{cm}, \quad (46)$$

and the constitutive behavior of its comprising phases is described by the dielectric Gent model, namely

$$\Psi^{(p)}(\mathbf{F}, \mathbf{D}) = -\frac{\mu^{(p)} J^{(p)}_m}{2} \ln\left(1 - \frac{I_1 - 3}{J^{(p)}_m}\right) + \frac{1}{2\varepsilon^{(p)}} I_{5e}. \quad (47)$$

The parameter $\mu^{(p)}$ is identified with the shear modulus in the limit of small strains. The parameter $J^{(p)}_m$ models the stiffening in elastomers when the strain they undergo approaches its limit (Gent 1996). The model parameters are set according to the properties of the commercial products Silicone CF19-2186 by Nusil and Fluorosilicone 730 by Dow-corning, as reported by Pelrine *et al* (2000b) and Dow-corning[3], respectively[4]. These parameters, together with the mass density and the dielectric strength—the limiting electric field, beyond

[3] http://www.centralcoating.com/wp-content/uploads/2014/11/Dow-Corning-730.pdf

[4] We have calculated J_m by estimating the limiting stretch using calculated the elongation at failure.

Table 1. Physical properties of Silicone CF19-2186 and Fluorosilicone 730.

Material	ρ (kg/m^3)	μ (kPa)	ε_r	J_m	Dielectric strength (MV/m)
(a) Silicone CF19-2186	1100	333	2.8	46.3	235
(b) Fluorosilicone 730	1400	167.67	7.11	6.28	372

which charge flows through the elastomer—are given in table 1.

As a benchmark, figure 2(a) displays the transmission characteristics of the film when no voltage is applied. Specifically, the blue and the black curves show the square of the transmission coefficient, T_m, and the localization factor γ, respectively, as functions of the frequency. Across the frequencies $2764-3887\frac{\text{rad}}{\text{s}}$ and $6112-7412\frac{\text{rad}}{\text{s}}$, two bandgaps are identified by positive values of γ, or, alternatively, vanishing values of T_m. In a periodic structure, bandgaps can also be identified by a Bloch-Floquet analysis. This approach requires solving an eigenvalue problem for the frequencies as functions of a so-called Bloch parameter k_B, within the irreducible first Brillouin zone $0 \leqslant k_B < \pi/l$, where $l = l^{(a)} + l^{(b)}$ (Kittel 2005, Farzbod and Leamy 2011). As a validation to our implementation of the scattering matrix, we have also carried out the Bloch-Floquet analysis. Accordingly, 2(b) shows the frequencies as functions of $k_B l$, using a Bloch-Floquet analysis of the hybrid matrix (Tan 2010). Indeed, the gaps observed in figure 2, i.e., the ranges of frequencies with no solution, are in agreement with the bandgaps observed in 2(a), thereby asserting the scheme used in calculating γ and T_m.

We examine next the transmission characteristics when the actuated phases are equally spaced. Specifically, in figure 3, the top (a–c), middle (d–f), and bottom (g–i) rows show the square of the transmission coefficient T_m (black curve) and the localization factor γ (blue curve), when the applied voltage equals $\Delta V = 5000$, 7000 and 10000 V, respectively. We note that the maximal voltage was chosen such that the resultant electric field remains below the limit posed by the dielectric strength. The first (a, d, g), second (b, e, h), and third (c, f, i) columns in figure 3 correspond to 9,6 and 4 actuated b-phases, respectively. We observe the opening of bandgaps within ranges of frequencies that are associated with the passbands when no voltage is applied. The number of these new gaps increases with the spacing between the actuated phases. For example, across the frequencies $2000-3000\frac{\text{rad}}{\text{s}}$, actuating 9 equi-spaced phases at $\Delta V = 10000$ V (figure 3(g)) introduces 3 new bandgaps at the intervals 632–862, 1328–1688, and $052-2404\frac{\text{rad}}{\text{s}}$; actuating 6 equi-spaced phases (figure 3(h)) presents 5 bandgaps at the intervals 450–562, 920–1118, 1412–1656, 1906–2158, and $2362-2574\frac{\text{rad}}{\text{s}}$; actuating 4 equi-spaced phases (figure 3(i)) opens 8 bandgaps at the intervals 316–370, 638–738, 966–1102, 1302–1460, 1638–1808, 1970–2138, 2280–2436, and 2544–2668 $\frac{\text{rad}}{\text{s}}$. In addition, increasing the number of actuated phases increases the localization of the evanescent modes, as inferred from the magnitude of the localization factor γ. By way of example, examine the largest value of γ at $\Delta V = 10000$ V: it equals $\gamma \simeq 0.8$, 0.72 and 0.69 when the number of actuated phases is 9 (figure 3(g)), 6 (figure 3(h)), and 9 (figure 3(i)), respectively. A similar trend of increase in γ is observed when the voltage is increased. For instance, a comparison between figures 3(a), (d) and (g) shows that when 9 phases are actuated at $\Delta V = 5000$, 7000 and 10000 V, the largest localization factor is is $\gamma \simeq 0.67$, 0.71 and 0.8, respectively. An exemplary comparison between the localization factor as function of the frequency between the different spacings is shown in figure 4(a). Specifically, the blue, brown, and black curves correspond to 9, 6 and 4 actuated (b)-phases, respectively, at $\Delta V = 10000$ V. As a benchmark, the red curve depicts the localization factor spectrum when no voltage is applied. An exemplary comparison between the localization factor as function of the frequency between the different magnitudes of voltage is shown in figure 4(b). Specifically, the black, brown and blue curves correspond to $\Delta V = 5000$, 7000 and 10000 V, respectively, when 9 phases are actuated. Again, as a benchmark, the red curve depicts the localization factor spectrum when no voltage is applied.

We explore next the transmission characteristics when the actuated cells are not spaced equally. We begin with actuations of successive cells. Thus, figure 5(a) shows T_m and γ as functions of the frequency, when phase b is actuated in cells 17–20. Specifically, the solid, dashed and dotted black (resp. blue) curves correspond to T_m (resp. γ) at $\Delta V = 10000$, 7000 and 5000 V, respectively. As a benchmark, the localization factor spectrum when the film is not actuated is denoted by the red curve, herein and throughout figure 5. It is shown that the gaps are rendered wider by the application of the voltage. As an example, observe that when $\Delta V = 10000$ V, the gaps are twice as wide when no voltage is applied. By contrast, we recall that equi-spaced actuation yielded the opening of new gaps, rather than extension of existing ones.

Figure 5(b) compares between the spectrum of T_m and γ when a different number of cells is activated. Specifically, the dotted, dashed and solid black (resp. blue) curves correspond to T_m (resp. γ) when phase b is actuated in cells 17–20, 16–21, and 14–23, respectively, with $\Delta V = 10000$ V. It is observed how increasing the number of actuated phases results with larger values of the localization factor, albeit maintaining the same gap widths, similarly to the role of ΔV.

Figure 5(c) displays a comparison of the transmission characteristics between different locations of an actuated stack of 10 cells. Specifically, the dashed and solid black (resp. dashed blue and brown) curves correspond to T_m (resp. γ) when phase b is actuated in cells 14–23 and 27–36, respectively, with $\Delta V = 10000$ V. The similarity between the

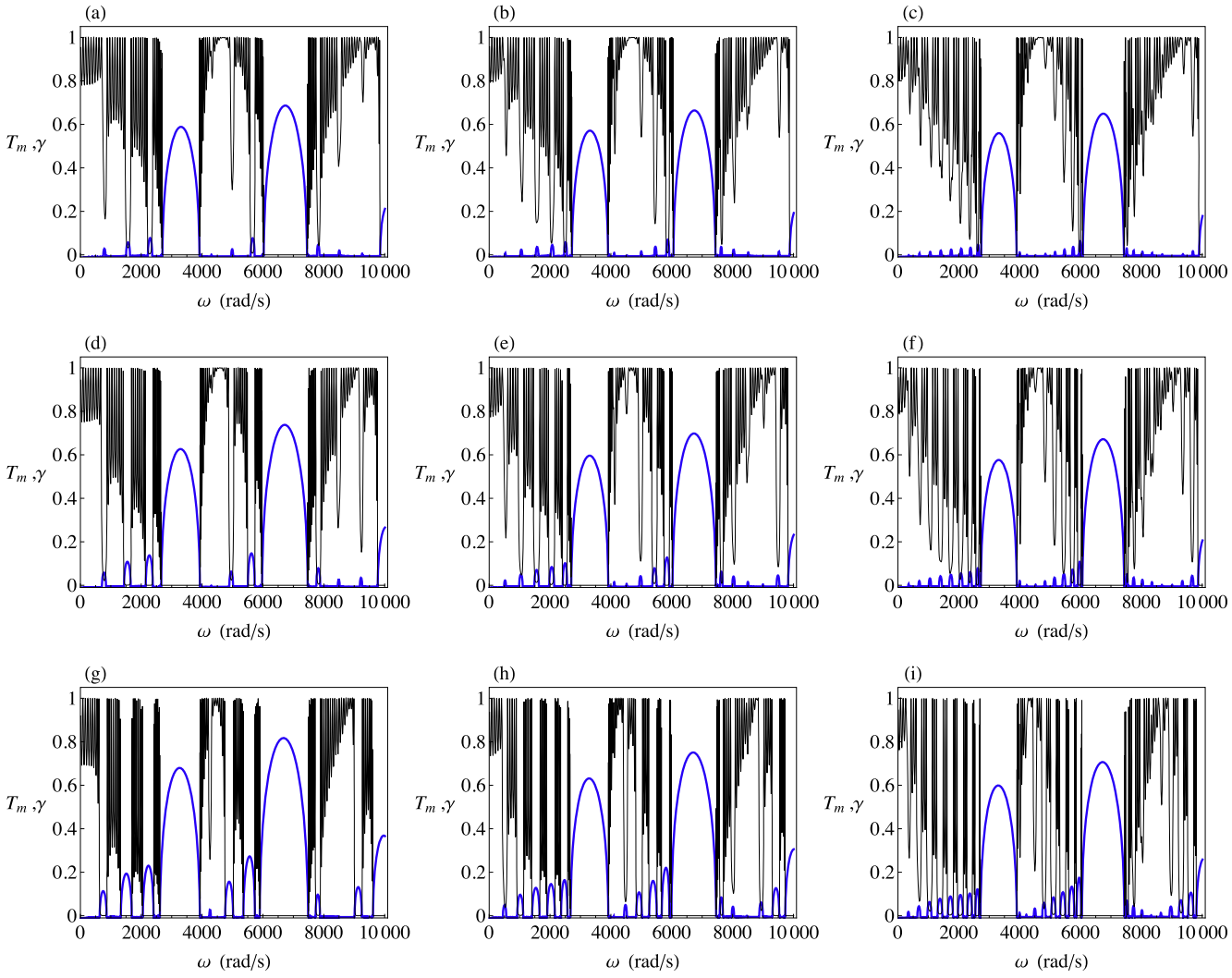

Figure 3. The coefficient T_m (black curves) and the localization factor γ (blue curves), when phases spaced at equal distances are actuated. The first, second, and third columns correspond to 9, 6 and 4 actuated *b*-phases, respectively; the top, middle, and bottom rows correspond to an applied voltage of $\Delta V = 5000$, 7000 and 10000 V, respectively.

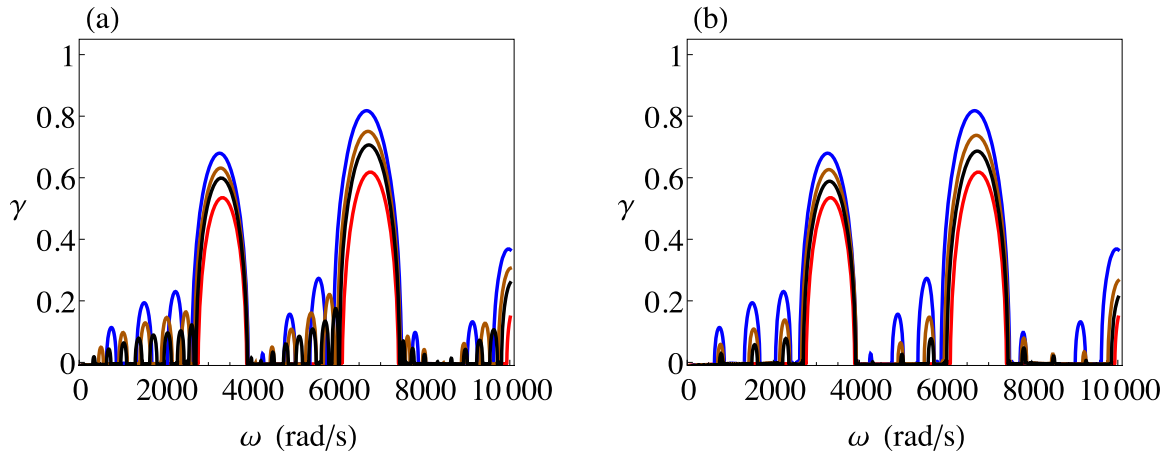

Figure 4. (a) The localization factor γ as function of the frequency ω at $\Delta V = 10000$ V. The blue, brown and black curves correspond to 9, 6 and 4 actuated *b*-phases, respectively. The red curve depicts the localization factor spectrum when no voltage is applied. (b) The localization factor γ as function of the frequency ω, when 9 phases are actuated. The red, black, brown and blue curves correspond to correspond to $\Delta V = 0$, 5000, 7000 and 10000 V, respectively.

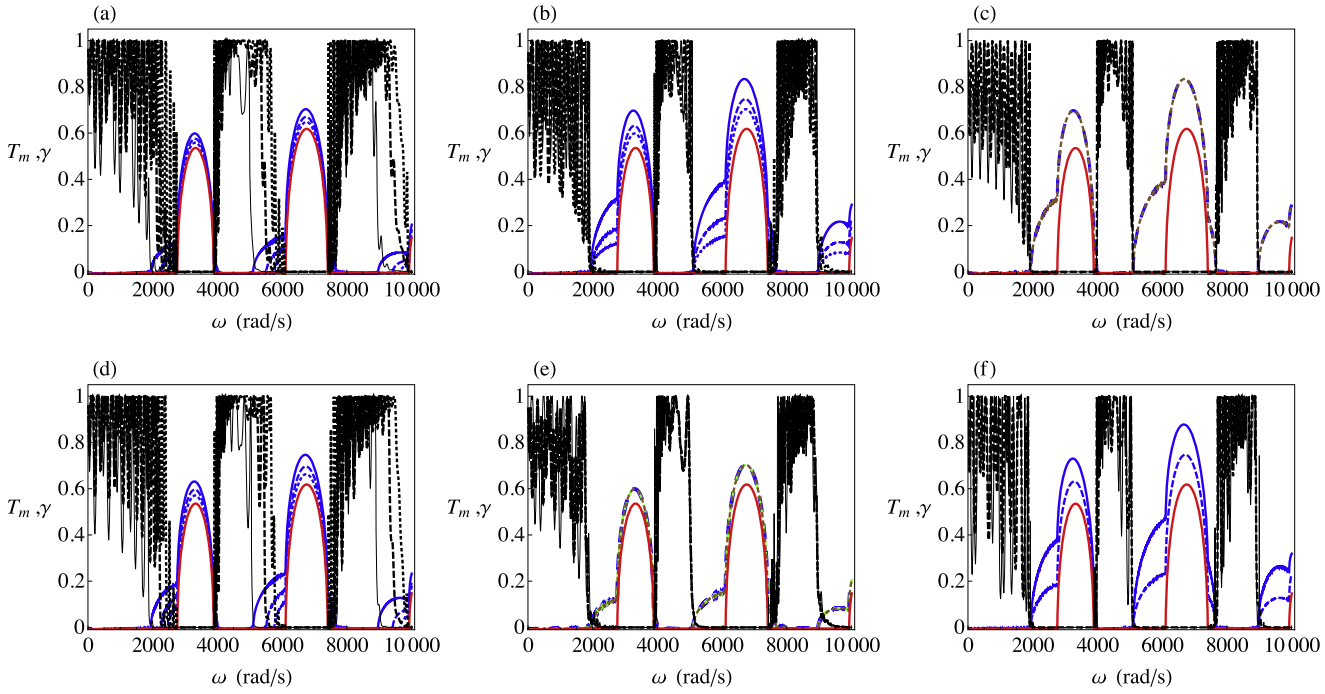

Figure 5. Transmission characteristics at different actuations. (a) The solid, dashed and dotted black (resp. blue) curves correspond to T_m (resp. γ) when phase b is actuated in cells 17-20 with $\Delta V = 10000$, 7000 and 5000 V, respectively. The localization factor spectrum when the film is not actuated is denoted by the red curve, herein and throughout figure 5. (b) The dotted, dashed and solid black (resp. blue) curves correspond to the T_m (resp. γ) when phase b is actuated in cells 17-20, 16-21, and 14-23, respectively, with $\Delta V = 10000$ V. (c) The dashed and solid black (resp. dashed blue and brown) curves correspond to T_m (resp. γ) when phase b is actuated in cells 14–23 and 27–36, respectively, with $\Delta V = 10000$ V. (d) The solid, dashed and dotted black (resp. blue) curves correspond to T_m (resp. γ) phase b in cells 16–21 is actuated with $\Delta V = 10000$, 7000 and 5000 V, respectively. (e) The dotted, dashed and solid black (resp. dashed brown, Green and blue) curves correspond to T_m (resp. γ) when phase b is actuated in cells 28–31, 6–9, and 17–20, respectively, with $\Delta V = 10000$ V. (f) The dashed black (resp. blue) curve corresponds to T_m (resp. γ) when phase b is actuated in cells 16–21. The solid curves correspond to the actuation of phase b in cells 4–9 and 19–24, with $\Delta V = 10000$ V.

curves implies that the location of the actuated stack does not significantly affect the transmission characteristics.

Figure 5(d) is the counterpart of 5(a), when the number of the actuated cells is 6. Thus, the solid, dashed and dotted black (resp. blue) curves correspond to T_m (resp. γ) phase b in cells 16–21 is actuated with $\Delta V = 10000$, 7000 and 5000 V, respectively. The trend observed in 5(a) is recovered, namely, wider gaps by the application of the voltage.

Figure 5(e) is the counterpart of 5(c), when the number of the actuated cells is 4. Accordingly, the dotted, dashed and solid black (resp. dashed brown, green and blue) curves correspond to T_m (resp. γ) when phase b is actuated in cells 28–31, 6–9 and 17–20, respectively, with $\Delta V = 10000$ V. Again, the location of the actuated stack has only a minor effect on the transmission characteristics.

Figure 5(f) compares the transmission characteristics between the actuations of a different number of stacks. Specifically, the dashed black (resp. blue) curve corresponds to T_m (resp. γ) when phase b is actuated in cells 16–21, whereas the solid curves correspond to the actuation of phase b in cells 4–9 and 19–24, with $\Delta V = 10000$V. It is observed that the spectrum of the localization factor does not differ much between the two configurations. The square of the transmission coefficient, however, is lowered by the actuation of additional stacks, particularly in the range $0 < \omega < 2000\frac{\text{rad}}{\text{s}}$.

We investigate next the transmission characteristics when considering nonconsecutive distributions of 6 actuated cells, at $\Delta V = 10000$ V. Figure 6(a) illustrates T_m (black curve) and γ (blue curve), when phase b is actuated in cells 13, 15, 17, 19, 21 and 23. For comparison, also displayed the localization factor when 6 equi-spaced cells are actuated (purple curve), when the stack comprising cells 16–21 is actuated (brown curve), and when no voltage is applied (red curve). The pattern of the resultant spectra is in-between the pattern of the equi-spaced actuation, and the pattern when successive cells were actuated. Thus, at one hand, we observe an extension of the gaps appearing in the periodic case, while this extension is not as wide as in the stacked case; at the other hand, we observe the opening of new gaps, however not as many as in the case of equi-spaced actuation.

We examine the spectra when changing the spacing between the second and the third actuated cells. Accordingly, figure 6(b) shows the spectrum of T_m (resp. γ) when phase b is actuated in cells 11, 13, 19, 21, 23 and 25. Comparing with figure 6(a), we observe more new gaps, and a lower localization factor across the extended frequencies of the two existing gaps. In contrast with the observed in figure 3, the localization factor does not change in an ordered manner between the new gaps.

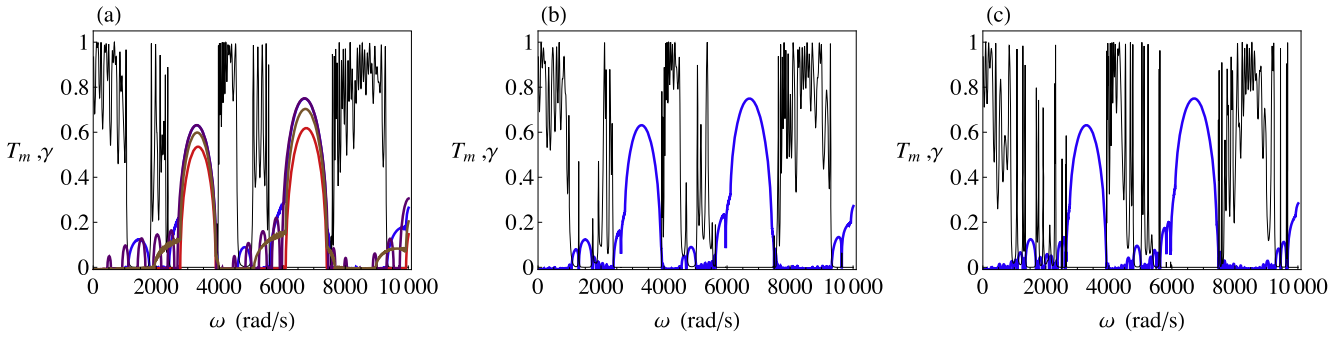

Figure 6. Transmission characteristics when actuating 6 cells in different aperiodic arrangements, at $\Delta V = 10000$ V. (a) The black (resp. blue) curve corresponds to T_m (resp. γ) when phase b is actuated in cells 13,15,17,19,21 and 23. The brown curve corresponds to the localization factor when phase b is actuated in cells 16–21. For comparison, also shown the localization factor when 6 equi-spaced cells are actuated (purple curve), and when the film is not actuated (red curve). (b) The coefficient T_m (resp. γ) when phase b is actuated in cells 11,13,19,21,23 and 25. (c) The black (resp. blue) curve corresponds to T_m (resp. γ) when phase b is actuated in cells 8, 10, 16, 20, 26 and 28.

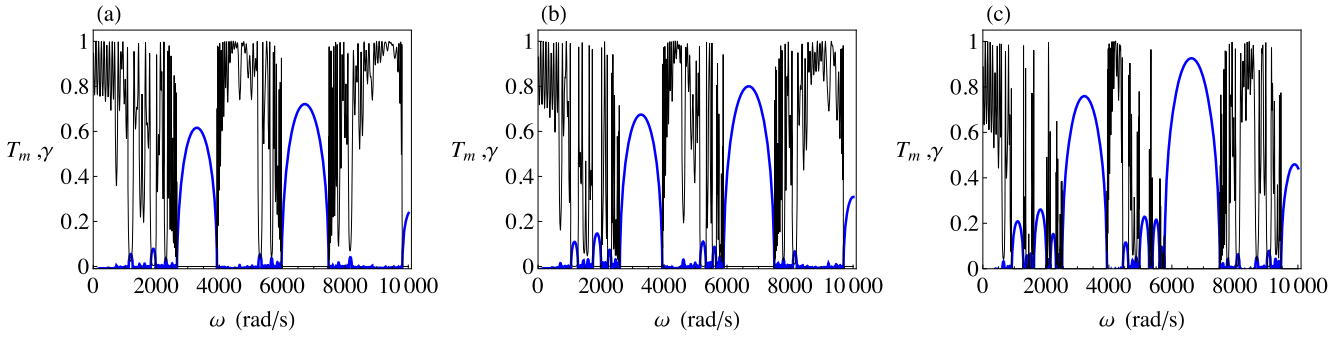

Figure 7. The spectrum of T_m (black curve) and γ (blue curve) of a film whose cells are subjected to (a) $\Delta V = 5000$ V, (b) 7000 V and (c) 10000 V, according to the Fibonacci rule.

We depart further from ordered aperiodicity, by considering the actuation of phase b in cells 8, 10, 16, 20, 26 and 28. Figure 6(c) displays the corresponding spectrum of T_m (black curve) and γ (blue curve). Therein, the gaps associated with those appearing when no voltage applied, are barely extended. Further, the number of new gaps is greater than in figure 6(b); the corresponding localization factor is lower than the localization factor across the new gaps in figure 6(b).

Finally, we evaluate next the transmission characteristics when the cells are actuated according to the standard Fibonacci sequence. Such a sequence is obtained by successively applying the substitution rule $U \to UO$, $O \to U$ to U, where U (resp. O) denotes a cell in which phase b is not activated (resp. activated). After the rule is applied 8 times, we obtain a pattern for a film consisting of 55 cells, from which we consider the first 36 cells. The corresponding coefficients T_m (black curve) and γ (blue curve) are depicted in figure 7. Specifically, figures 7(a), (b), and (c) correspond to an applied voltage of $\Delta V = 5000$, 7000 and 10000 V, respectively.

The spectrum structure of the Fibonacci film is in-between the spectrum structure of a film whose actuated phases are equi-spaced (figure 3), and a film whose actuated phases were chosen without order (figure 6(c)). As such, it is characterized by the opening of new bandgaps—not the extension of bandgaps—within intervals associated with passbands when no voltage is applied. Contrarily to the trend in figure 3, the magnitude of γ at the new gaps does not vary monotonically, however, not as disorderedly as in figure 6(c). Consider, by way of example, the new gap whose central frequency is about $2000\frac{\text{rad}}{\text{s}}$ in figure 7(c); its localization factor is $\gamma \cong 0.23$, the localization factor of the gaps in its close vicinity is $\gamma \cong 0.05$, while the localization factor of the next gaps to the left and to the right are 0.2 and 0.15, respectively. A comparison between the spectra at the different voltages shows that as the voltage is increased, the magnitude of localization factor becomes larger, as expected.

6. Summary

We have introduced a new strategy to manipulate flexural waves in thin elastomeric films, based on electrostatically controlled mode localization. To this end, we have first determined analytically the response of a two-component film to a combination of an axial force and applied voltage. The considered actuation scheme enables the application of voltage to each phase separately, and hence introduces controlled aperiodicity to the film. We have then employed a structural approach to investigate the response of the actuated film to small flexural excitations. Specifically, we have developed the counterpart of the Euler–Bernoulli governing equation, when the finite deformation and stiffening of the film were

considered. Accounting for the incompressibility constraint, we have showed that the instantaneous structural stiffness depends on the boundary conditions, and cannot be determined solely from the constitutive law. To study the dynamics, we have adapted a stable matrix method, which was originally developed for the Sturm-Liouville equation.

We have evaluated the transmission characteristics of an exemplary film, when examining different arrangements of actuated phases, at different magnitudes of voltage. The computational investigation has shown that each type of aperiodicity causes a different kind of mode localization. Specifically, when phases spaced at equal distances are actuated, patterned new gaps open within ranges of frequencies that are associated with the passbands of the film in the absence of charge; when a stack of adjacent cells is actuated, existing gaps are rendered wider; when the actuation creates aperiodicity without order, numerous new gaps of low localization factor open, without a pattern in their relative location and decay rate; when the actuation follows the Fibonacci sequence, the transmission characteristics are in-between the characteristics the case of unordered aperiodicity, and the characteristics the case of ordered actuation. In all of the arrangements, localization has increased by the amplification of the voltage; this increase is quantified by the localization factor of existing gaps, and the opening of new ones.

Our findings demonstrate that electrostatically controlled aperiodicity can be exploited to actively control elastic waves in elastomeric films. Hence, a new approach for the design of active waveguides, filters, and motion control is introduced.

Acknowledgments

GS acknowledges BSF (Grant No. 2014358) and ISF (Grant No. 1912/15) supports. GS also thanks Prof. Eng Leong Tan for helpful discussions on the hybrid method. RPS acknowledges postdoctoral grant from PRODEP (No. DSA/103.5/16/9408).

References

Anderson I A, Gisby T A, McKay T G, O'Brien B M and Calius E P 2012 Multi-functional dielectric elastomer artificial muscles for soft and smart machines *J. Appl. Phys.* **112** 041101

Babaee S, Viard N, Wang P, Fang N X and Bertoldi K 2016 Harnessing deformation to switch on and off the propagation of sound *Adv. Mater.* **8** 1631–5

Bayat A and Gordaninejad F 2015 Dynamic response of a tunable phononic crystal under applied mechanical and magnetic loadings *Smart Mater. Struct.* **24** 065027

Bendiksen O O 2000 Localization phenomena in structural dynamics *Chaos Solitons Fractals* **11** 1621–60

Bertoldi K and Boyce M C 2008 Wave propagation and instabilities in monolithic and periodically structured elastomeric materials undergoing large deformations *Phys. Rev.* B **78** 184107

Carta G and Brun M 2015 Bloch-floquet waves in flexural systems with continuous and discrete elements *Mech. Mater.* **87** 11–26

Castañeda P P and Siboni M H 2012 A finite-strain constitutive theory for electro-active polymer composites via homogenization *Int. J. Non-Linear. Mech.* **47** 293–306

Cohen N, Dayal K and deBotton G 2016 Electroelasticity of polymer networks *J. Mech. Phys. Solids* **92** 105–26

Cohen N and deBotton G 2014 Multiscale analysis of the electromechanical coupling in dielectric elastomers *European Journal of Mechanics—A/Solids* **48** 48–59 Frontiers in Finite-Deformation Electromechanics

deBotton G, Tevet-Deree L and Socolsky E A 2007 Electroactive heterogeneous polymers: analysis and applications to laminated composites *Mech. Adv. Mater. Struct.* **14** 13–22

Degraeve S, Granger C, Dubus B, Vasseur J O, Thi M P and Hladky A-C 2015 Tunability of bragg band gaps in one-dimensional piezoelectric phononic crystals using external capacitances *Smart Mater. Struct.* **24** 085013

Díaz-Calleja R and Riande E 2013 Comments on the influence of stretching on the permittivity of dielectric elastomers *Smart Mater. Struct.* **22** 038001

Dorfmann A and Ogden R W 2005 Nonlinear electroelasticity *Acta. Mech.* **174** 167–83

Dorfmann A and Ogden R W 2010 Electroelastic waves in a finitely deformed electroactive material *IMA. J. Appl. Math.* **75** 603–36

Farzbod F and Leamy M J 2011 Analysis of bloch's method and the propagation technique in periodic structures *Journal of Vibration and Acoustics* **133** 031010

Gei M, Colonnelli S and Springhetti R 2014 The role of electrostriction on the stability of dielectric elastomer actuators *Int. J. Solids Struct.* **51** 848–60

Gei M, Roccabianca S and Bacca M 2011 Controlling bandgap in electroactive polymer-based structures *IEEE-ASME Trans. Mechatronics* **16** 102–7

Gent A N 1996 A new constitutive relation for rubber *Rubber Chem. Technol.* **69** 59–61

Graff K F 1975 Wave motion in elastic solids *Dover Books on Physics Series* (New York: Dover Publications) ISBN 9780486667454

Hodges C H 1982 Confinement of vibration by structural irregularity *J. Sound Vib.* **82** 411–24

Jia K, Wang M, Lu T, Zhang J and Wang T 2016 Band-gap tunable dielectric elastomer filter for low frequency noise *Smart Mater. Struct.* **25** 055047

Kissel G J 1991 Localization factor for multichannel disordered systems *Phys. Rev.* A **44** 1008–14

Kittel C 2005 *Introduction to Solid State Physics* (Hoboken, NJ: John Wiley & Sons, Inc.)

Ko D Y K and Sambles J R 1988 Scattering matrix method for propagation of radiation in stratified media: attenuated total reflection studies of liquid crystals *J. Opt. Soc. Am.* A **5** 1863–6

Kofod G 2008 The static actuation of dielectric elastomer actuators: how does pre-stretch improve actuation? *J. Phys. D: Appl. Phys.* **41** 215–405

Kushwaha M S, Halevi P, Dobrzynski L and Djafari-Rouhani B 1993 Acoustic band structure of periodic elastic composites *Phys. Rev. Lett.* **71** 2022–5

Liu L 2013 On energy formulations of electrostatics for continuum media *J. Mech. Phys. Solids* **61** 968–90

Liu Y, Liu L, Zhang Z and Leng J 2009 Dielectric elastomer film actuators: characterization, experiment and analysis *Smart Mater. Struct.* **18** 095024

Maciá E 2012 Exploiting aperiodic designs in nanophotonic devices *Rep. Prog. Phys.* **75** 036502

McMeeking R M and Landis C M 2005 Electrostatic forces and stored energy for deformable dielectric materials *J. Appl. Mech., Trans. ASME* **72** 581–90

Nakamura K 1996 Elastic wave energy-trapping and its application to piezoelectric devices *Electronics and Communications in Japan (Part II: Electronics)* **79** 30–9

Onal C D and Rus D 2013 Autonomous undulatory serpentine locomotion utilizing body dynamics of a fluidic soft robot *Bioinspiration and Biomimetics* **8** 026003

Pelrine R, Kornbluh R, Joseph J, Heydt R, Pei Q-B and Chiba A 2000b High-field deformation of elastomeric dielectrics for actuators *Mater. Sci. Eng.* **11** 89–100

Pelrine R, Kornbluh R, Pei Q-B and Joseph J 2000a High-speed electrically actuated elastomers with strain greater than 100% *Sci.* **287** 836–9

Pelrine R E, Kornbluh R D and Joseph J P 1998 Electrostriction of polymer dielectrics with compliant electrodes as a mean of actuation *Sensors Actuators* A **64** 77–85

Pérez-Álvarez R and García-Moliner F 2004 Transfer Matrix, Green Function and related techniques: tools for the study of multilayer heterostructures *Universitat Jaume I* (Spain: Castellón de la Plana)

Pérez-Álvarez R, Pernas-Salomón R and Velasco V R 2015 Relations between transfer matrices and numerical stability analysis to avoid the ωd problem *SIAM J. Appl. Math.* **75** 1403–23

Pernas-Salomón R, Pérez-Álvarez R, Lazcano Z and Arriaga J 2015 The scattering matrix approach: a study of elastic waves propagation in one-dimensional disordered phononic crystals *J. Appl. Phys.* **118** 234302

Rokhlin S I and Wang L 2002 Stable recursive algorithm for elastic wave propagation in layered anisotropic media: Stiffness matrix method *The Journal of the Acoustical Society of America* **112** 822

Ruzzene M and Baz A 1999 Control of wave propagation in periodic composite rods using shape memory inserts *Journal of Vibration and Acoustics* **122** 151–9 06

Shmuel G 2013 Electrostatically tunable band gaps in finitely extensible dielectric elastomer fiber composites *Int. J. Solids Struct.* **50** 680–6

Shmuel G 2015 Manipulating torsional motions of soft dielectric tubes *J. Appl. Phys.* **117** 174902

Shmuel G and deBotton G 2012 Band-gaps in electrostatically controlled dielectric laminates subjected to incremental shear motions *J. Mech. Phys. Solids* **60** 1970–81

Shmuel G and deBotton G 2013 Axisymmetric wave propagation in finitely deformed dielectric elastomer tubes *Proc. of the Royal Society A: Mathematical, Physical and Engineering Science* **469** 20130071

Shmuel G, Gei M and deBotton G 2012 The Rayleigh-Lamb wave propagation in dielectric elastomer layers subjected to large deformations *Int. J. Non-Linear. Mech.* **47** 307–16

Sigalas M M and Economou E N 1992 Elastic and acoustic wave band structure *J. Sound Vib.* **158** 377–82

Sik Ma P, Kwon Y E and Kim Y Y 2013 Wave dispersion tailoring in an elastic waveguide by phononic crystals *Appl. Phys. Lett.* **103** 151901

Sun W, Liu F, Ma Z, Li C and Zhou J 2016 Soft mobile robots driven by foldable dielectric elastomer actuators *J. Appl. Phys.* **120** 084901

Suo Z, Zhao X and Greene W H 2008 A nonlinear field theory of deformable dielectrics *J. Mech. Phys. Solids.* **56** 467–86

Tan E L 2006 Hybrid compliance-stiffness matrix method for stable analysis of elastic wave propagation in multilayered anisotropic media *The Journal of the Acoustical Society of America* **119** 45–53

Tan E L 2010 Generalized eigenproblem of hybrid matrix for floquet wave propagation in one-dimensional phononic crystals with solids and fluids *Ultrasonics* **50** 91–8

Toupin R A 1963 A dynamical theory of elastic dielectrics *Int. J. Engineering Science* **1** 101–126

Treloar L R G 1975 *The Physics of Rubber Elasticity* (Oxford: Clarendon Press)

Tröls A, Kogler A, Baumgartner R, Kaltseis R, Keplinger C, Schwödiauer R, Graz I and Bauer S 2013 Stretch dependence of the electrical breakdown strength and dielectric constant of dielectric elastomers *Smart Mater. Struct.* **22** 104012

Wu L-Y, Wu M-L and Chen L-W 2009 The narrow pass band filter of tunable 1d phononic crystals with a dielectric elastomer layer *Smart Mater. Struct.* **18** 015011

Yang W-P and Chen L-W 2008 The tunable acoustic band gaps of two-dimensional phononic crystals with a dielectric elastomer cylindrical actuator *Smart Mater. Struct.* **17** 015011

Yi K, Collet M, Ichchou M and Li L 2016 Flexural waves focusing through shunted piezoelectric patches *Smart Mater. Struct.* **25** 075007

Yin J, Peng H J, Zhang S, Zhang H W and Chen B S 2015 Design of nacreous composite material for vibration isolation based on band gap manipulation *Comput. Mater. Sci.* **102** 126–34

Zhang J, Chen H, Li B, McCoul D and Pei Q 2015 Tunable active vibration attenuation using highly deformable dielectric elastomers *Smart Mater. Struct.* **24** 115033

Zhou X and Chen C 2013 Tuning the locally resonant phononic band structures of two-dimensional periodic electroactive composites *Physica B: Condensed Matter* **431** 23–31